physica status solidi (a)

RESEARCH ARTICLE OPEN ACCESS

Closing the Loop: Italian Waste Biomass as a Sustainable Source for Sodium-Ion Battery Anodes

Valerio C. A. Ficca[1] | Alessandra Del Giudice[2] | Maria Di Pea[1,3] | Leonardo Duranti[4] | Luca Mesina[1,3] | Ernesto Placidi[5] | Alessandro Dell'Era[6] | Sergio Brutti[2] | Claudia Paoletti[1] | Giovanni B. Appetecchi[1] | Giorgia Greco[1]

[1]ENEA (Italian National Agency for New Technologies, Energy and Sustainable Economic Development), Department of Energy Technologies and Renewable Sources (TERIN), Division of Technologies and Vectors for Decarbonization (DEC), Laboratory of Technologies and Devices for Electrochemical Storage (ACEL), Casaccia Research Centre, Rome, Italy | [2]Department of Chemistry, Sapienza University of Rome, Rome, Italy | [3]Department of Chemical Engineering Materials Environment, Sapienza University of Rome, Rome, Italy | [4]Department of Chemical Sciences and Technologies, University of Rome Tor Vergata, Rome, Italy | [5]Department of Physics, Sapienza University of Rome, Rome, Italy | [6]Department of Basic and Applied Sciences for Engineering (SBAI), Sapienza University of Rome, Rome, Italy

Correspondence: Valerio C. A. Ficca (valerio.ficca@enea.it)

Received: 31 October 2025 | **Revised:** 12 February 2026 | **Accepted:** 22 February 2026

Keywords: biowaste resources | circular economy | electrochemical performance | hard carbons | sodium-ion batteries

ABSTRACT

Developing a sustainable circular economy requires specific protocols to produce sustainable energy materials for renewable energy deployment. Sodium-ion batteries (SIBs) offer a safer and cheaper alternative to lithium-ion batteries, but their performance is limited by anode materials. Here, we investigate hard carbons (HCs) derived from three Italian waste biomasses: hazelnut shells, wild giant cane, and olive stones, comparing them to commercially available petroleum-based HC. A facile and eco-friendly synthesis involving ball milling, citric acid digestion, and pyrolysis at 1100°C yields nanostructured active materials for SIBs. We analyze their morphology, porosity, microstructure, defectivity, surface chemistry, and electrochemical performance. Results reveal that the biomass-derived HCs exhibit comparable performance to the commercial counterpart. The wild giant cane and olive stone-derived HCs show the best electrochemical performance, offering a promising route toward sustainable and high-performance SIB anodes.

1 | Introduction

The route set by the European Commission (EU) to ferry the eurozone into a more sustainable and affordable world is based on new paradigms that were not fully internalized in the pre-COVID era. Nowadays, the current economy and energy scenarios are still heavily reliant on fossil fuels and on the "take-make-waste" model used since the last industrial revolution. To overcome this outdated concept, the upcoming EU Circular Economy Act [1] targeting high-impact sectors such as agriculture, energy, and electronics, aims at creating a market for waste and secondary materials within the EU economy, will develop all the prerequisites for renewable, efficient, and profitable economy and energy systems. Indeed, one of the act's mandates is to transform waste streams into high-value secondary raw materials, supporting local supply chains to reduce carbon footprints and creating new industrial partnership among sectors and the green energy industry. Particularly, the goal is to foster markets for secondary raw materials like those in the critical raw materials (CRM) Act where, by 2030, at least 25% of the EU's strategic raw material consumption must come from recycling and 40% from domestic processing, hence boosting the use of recycled components in general, especially to support the climate neutrality set for 2050. Indeed, the use of a more sustainable and circular model is mandatory to reduce the anthropogenic carbon footprint on the ecosystem, especially in heavily pollutant sectors like transportation and manufacturing. However, the use of renewable energy is still hindered by drawbacks associated with the intermittent nature and high upfront costs of the technologies. In this context, the main research activity of the energy sector is centered around the replacement of expensive and less affordable elements like rare earth elements (REE), noble metals, Co, Li, etc. with cheaper and more abundant ones, but maintaining performances.

Electrochemical energy storage (EES) technologies have been revolutionized by intercalation batteries, particularly lithium-ion batteries (LIBs), which have seen widespread commercialization since the 1990s. However, the increasing global demand for Li, coupled with its uneven distribution in the Earth's crust, is causing supply concerns. This necessitates the exploration of alternative EES systems based on more abundant and readily available elements to reduce reliance on CRMs.

Sodium-ion batteries (SIB) are a suitable alternative to LIBs since they are based on the same working principle. Compared to Li, Na possesses similar physical and chemical properties, higher abundance, wider distribution around the planet, and thus lower costs [2–4]. Unfortunately, SIB possess also lower energy density respect to the Li counterpart, due to a lower oxidation potential and higher atomic weight of Na, and to less optimized active materials [5, 6]. Nevertheless, SIB are more suitable in colder areas [7] and can still be used for stationary grid energy storage where dimensions are not a limiting factor, or for light transportation [5, 6]. Similar to LIB, SIBs are based on the phenomenon of Na^+ ion transport back and forth during discharge/charge cycles between a cathode and an anode separated by a suitable electrolyte. Different types of cathodic materials have been developed with good results, such as layered oxides, polyanion compounds, and Prussian blue analogues [8–10], but the anodic counterpart is still considered the bottleneck of the system, affecting the rate of discharge and the total coulombic efficiency [5].

Among the anodic materials [11], carbon-based structures are considered the most promising, since already used in LIB as graphite, but especially due to the large availability of C compounds and chemical stability of its allotropes. Carbonaceous materials are also less prone to volume expansion upon operation. Different than LIB, where Li^+ ion is easily intercalated into active materials, graphite is not applicable in SIB because of thermodynamical instability related to the intercalation process [12, 13]. Other phenomena are thus related to Na^+ ion storage, such as adsorption, insertion, and clustering over partially ordered graphitic structures, called hard carbons (HC) [14–18].

HC belong to the sub-class of carbon materials unable to fully graphitize even at the highest temperature of 3000°C [19]. This is mainly because of the precursors used for the synthesis, characterized by a high degree of crosslinked structures that hinder the graphitic domains' rearrangement upon heating. HC are thus composed of locally ordered graphitic crystallites into an amorphous phase possessing intrinsic porosity [19]. HCs for SIB are usually produced by means of high-temperature treatments in controlled atmosphere; the precursors used are low-cost compounds, such as glucose and polymers, or biowaste, subtracting carbon species that would be discarded into the atmosphere as CO_2 emissions, supporting thus the circular economy. The use of biowaste within the framework of the upcoming EU Circular Economy Act directly motivates the research on SIB anodes by creating a demand for sustainable local resources like secondary raw materials and a strategic reduction of dependence on imported electroactive components. Common biomass precursors effectively used for HC synthesis at temperatures up to 1700°C are sugarcane bagasse, vine shoots, walnut shell, hazelnut shells, wheat straw, bamboo, macadamia nutshell, rice husk, peanut shells, green peas, and corncob [20–31], obtaining performances in terms of specific capacity between 200 and 350 mAh g^{-1} at various galvanostatic rates. Despite the economic and societal effects of using biowaste, biomass precursors are particularly interesting for HC synthesis due to the presence of cellulose, hemicellulose, and lignin, possessing intrinsic microstructure, channels, and crosslinked structural units that can be retained upon high-temperature pyrolysis [5, 19]. A proper interconnected porous structure is essential to the Na^+ ion transport from the electrolyte solution to the bulk of the HC, directly affecting the performance of the system. Electronic conductivity, in terms of graphitic content, plays also a fundamental role, along with a suitable defectivity capable of reversible hosting the Na^+ ions, and a thin stable solid electrolyte interface (SEI). It is thus straightforward that a proper design of anodic active material is essential to boost performance of SIB and make a step forward towards a more sustainable and greener world.

Herein, we present a comparison of a commercial petroleum-based HC with three HC obtained with three different waste biomasses (bio-HC) commonly found in the Italian peninsula: hazelnut shells, wild giant cane, and olive stones. Upon a facile and ecofriendly synthesis procedure based on ball milling, citric acid digestion, and pyrolysis at 1100°C, it was possible to obtain a suitable nanostructured active material for SIB, obtaining peculiar properties investigated in terms of morphology, porosity, microstructure, defectivity, surface chemistry, and electrochemical performance.

2 | Results

The synthesis of the bio-HC, without any other preparation of the precursors, started with a ball milling grinding to obtain a fine dispersed powder. The three biomasses, hazelnut shells (HZN), wild giant cane (CAN), and olive stones (OLV), were processed as follows. First, they underwent autoclave digestion to facilitate the decomposition of the natural macromolecular compounds. This was followed by a one-step pyrolysis at 1100°C. The results of each step were then investigated using scanning electron microscope (SEM) to observe the morphology and evaluate the presence of contaminants through energy-dispersive X-ray spectroscopy (EDX). Figures S1, S2, and 1 report the SEM images of the bio-HC obtained, respectively, after the ball milling, the autoclave digestion, and the pyrolysis step, along with a commercial hard carbon (HCcom). In Table S1–S3, the summary of the EDX analysis is reported.

After ball milling, all three samples were successfully ground into micrometric fragments with irregular size and shape. CAN shows the presence of fiber-like structures, typical of the *Arundo donax* wild giant cane [32]. The details at higher magnification (Figure S1b,d,f) clearly exhibit the presence of a dense polymer-like film, smoothing the samples surface, likely consisting of natural compounds matrix still present in the nontreated samples. K and Ca were revealed in traces in the ball-milled samples (Table S1), while Si impurities (1.2 ± 0.5 wt.%) were only found in CAN sample. The effects of citric acid digestion are clear in

Figure S2, and all samples show rougher surfaces and increased porosity following partial decomposition of the organic film observed in Figure S1. Globular features are visible in the higher-magnification images of Figure S2d,f, likely due to residual hemicellulose [33]. EDX analysis reported in Table S2 revealed the absence of contaminants after digestion except for CAN and the C:O ratio increased, as compared to that observed for the ball-milled samples. Figure 1 shows the samples after the pyrolysis step, along with HCcom. After pyrolysis, all bio-HC samples display increased porosity. At lower magnification, fiber-like

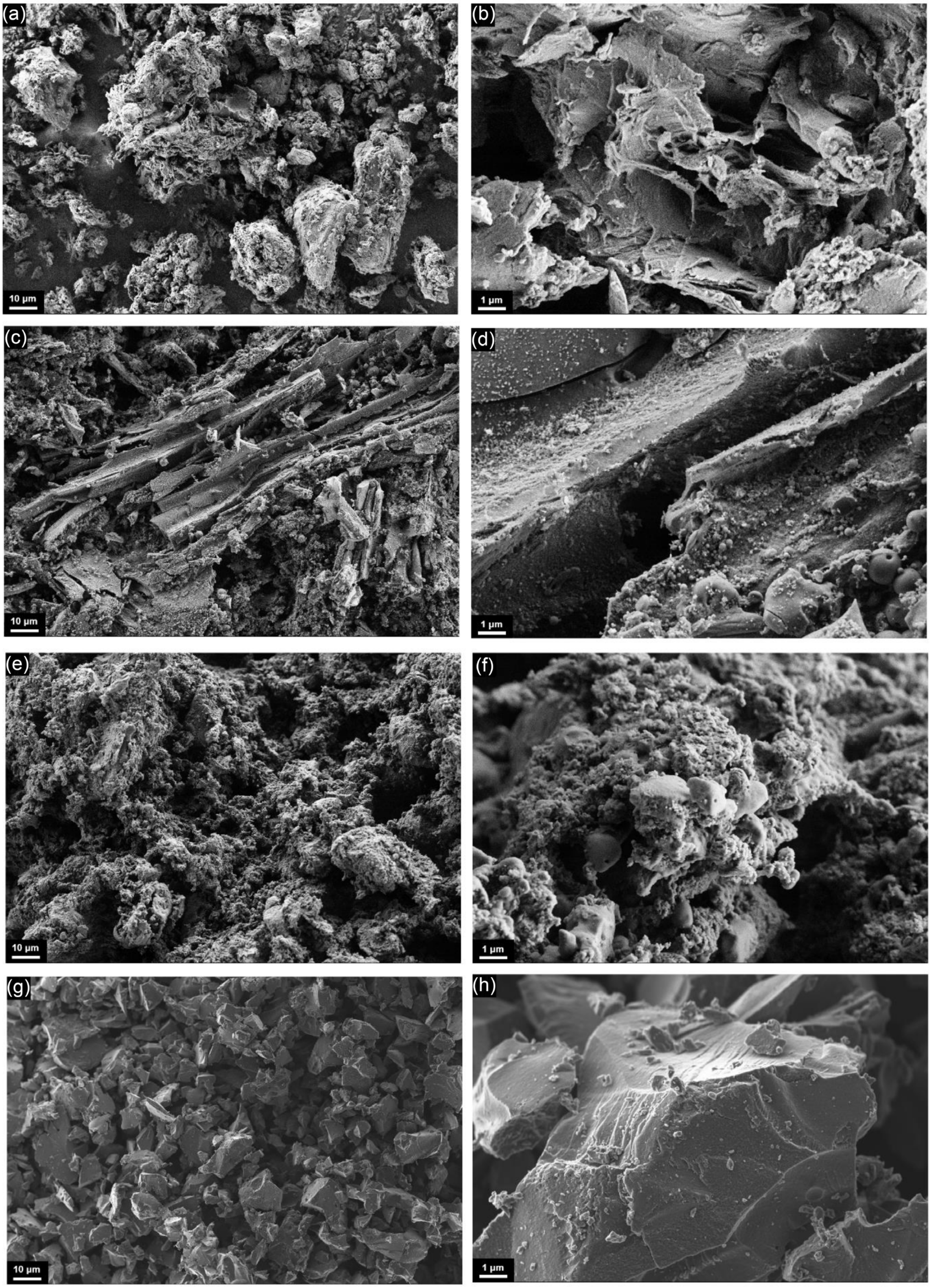

FIGURE 1 | SEM micrographs at different magnifications of the pyrolyzed samples and the commercial hard carbon: (a,b) HZN, (c,d) CAN, (e,f) OLV; (g,h) HCcom.

structures are still visible in CAN, while HZN and OLV show irregularly shaped particles, with OLV featuring the smallest and finest distributed pores. Conversely, HCcom consists of large, compact, and bulk fragments with a more homogeneous surface texture. According to EDX results reported in Table S3, as expected, the carbon content increased by over 95 wt.% in bio-HC pyrolyzed samples.

To further investigate the porosity, the microstructure, the defectivity, and the surface chemistry of the samples, of paramount importance for an effective and reversible Na^+ ion shuttling, small-angle X-ray scattering (SAXS), X-ray powder diffraction (XRD), Raman, and X-ray photoemission spectroscopy (XPS) were carried out. The main results are summarized in Figure 2. SAXS measurements were carried out to identify the structural differences among the samples. The SAXS intensity profiles reported in the log–log plot (Figure 2a) show distinct trends among the samples. HCcom exhibits a steeper intensity decay at intermediate q values, indicative of a smoother surface morphology and lower surface fractal dimension. This behavior is consistent with its petrochemical origin and high-temperature pyrolysis (>1500°C), which leads to a more compact and ordered carbon matrix, as observed in SEM images. In contrast, the bio-HC samples display higher intensity at low q values, suggesting increased surface roughness and larger specific surface area. This is in agreement with the SEM images, which reveal more irregular and defective surfaces, particularly in the CAN and OLV samples. The power-law behavior observed in this range is typical of surface fractals and confirms the presence of multiscale roughness, a structural trait often found in HCs obtained from biomass via lower-temperature pyrolysis processes (~1100°C) [34]. The Kratky representation (Figure S3), which enhances features associated with nanopore distributions and internal structural ordering, shows broad humps centered around $q \approx 2\ \mathrm{nm}^{-1}$ for all samples. This signal is attributed to the presence of nanopores in the 2–3 nm range. The bump is more pronounced and slightly shifted in HCcom, indicating a narrower distribution and possibly larger pore compared to the bio-derived samples. The broader and flatter features observed for the bio-HCs suggest a more heterogeneous distribution of smaller pores, consistent with a less graphitized and more disordered structure. These findings align with previous reports highlighting that biomass-derived hard carbons tend to possess a more complex microporous network and higher surface roughness, which can enhance sodium storage by providing more active sites but may also require careful electrolyte tuning to control SEI formation and minimize irreversible capacity [35]. Therefore, the SAXS data provide critical insight into how the origin of the precursor and the processing conditions affect the nanoscale architecture of HCs. This has direct implications for their performance as anode materials in sodium-ion batteries [36]. XRD is a non-destructive bulk technique that is highly useful for characterizing the structural parameters of amorphous carbons. The XRD pattern of hard carbon typically shows two broad diffraction peaks centered approximately at $2\theta \approx 23°$ and 43°, corresponding to the (002) and (10) planes of turbostratic carbon, respectively. These peaks are broad and of low intensity due to the absence of long-range crystalline order and the predominance of an amorphous structure with limited graphitic stacking. This signature is characteristic of hard carbon

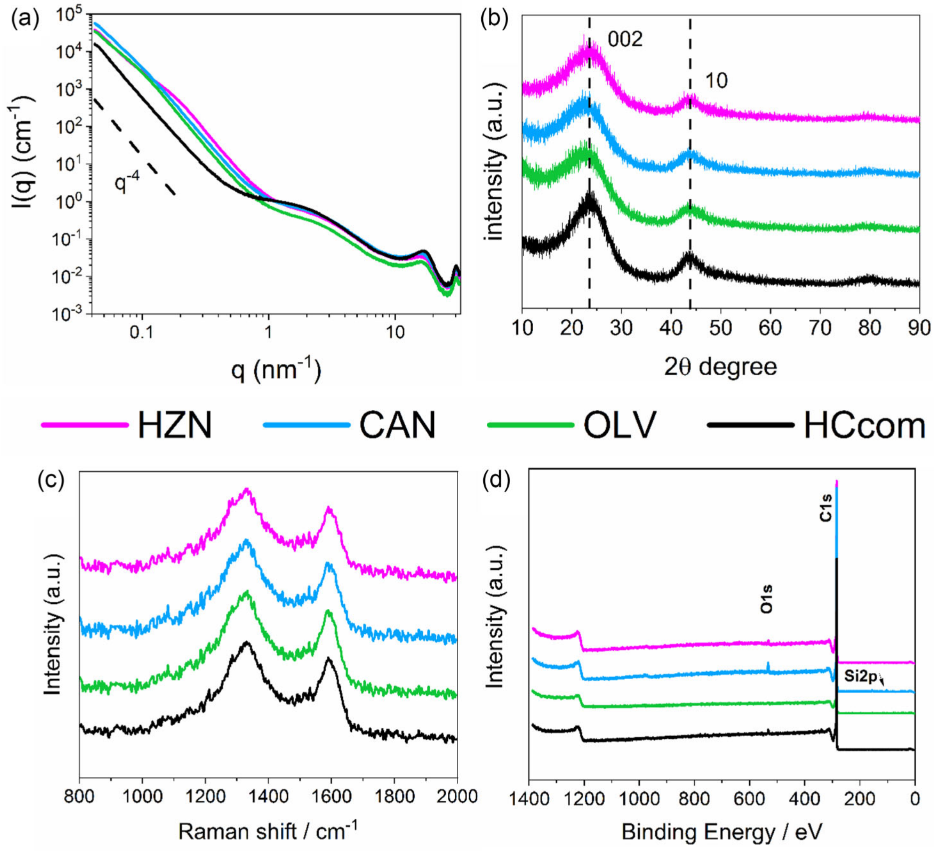

FIGURE 2 | Material Characterization comparison of the prepared samples. (a) SAXS profile, (b) XRD spectra, (c) Raman spectra, and (d) XPS survey spectra.

materials derived from biomass precursors, for which such broad features and relatively large (>0.335 nm) interlayer spacings (a_3) are commonly reported [37]. For carbon materials, the Bragg equation is used to determine interlayer distances from the position of the (002) reflection, while the Scherrer equation provides estimates of the stacking height and lateral size of graphene layers [36, 38–40]. However, as mentioned above, due to the high structural disorder in these materials, the application of Bragg and Scherrer relations is limited: the peak broadening and asymmetry prevent accurate determination of peak maxima, and these equations do not account for curvature or defects that strongly affect the structure. To overcome these limitations in analyzing the disordered carbon materials, we employed the Ruland and Smarsly algorithm [41], implemented via the OctCarb script, to quantitatively analyze our XRD patterns. This approach allows for a more accurate determination of structural parameters by considering the entire diffraction pattern rather than relying on isolated reflections [42]. The results of these fitting procedures (reported in Figure S4 and summarized in Table S4) revealed a trend in the in-plane crystallite sizes (L_a) of the bio-HC materials, with HZN < OLV < CAN, while the average stack height (L_c) was comparable among the samples. At the same time, the average chord lengths (l_m) followed a different trend with OLV < HZN < CAN, consistent with their highly local disordered and amorphous structures. On the contrary, the petroleum-derived HC exhibits significantly larger La and longer lm due to the higher degree of ordering within the sp^2 domains and a more extended aromatic network. Interestingly, regarding the interlayer spacings (a_3), the trend observed was HZN < OLV < HCcom < CAN, again with CAN possessing the highest value of 0.381 nm. Finally, the average C—C bond length (lcc) was found to be comparable among all the four samples. Lastly, the average number of graphene layers per stack (N) is maximum for HCcom (4) and slightly lower for the bio-HC (HZN < CAN < OLV). The reduced average stacking number ($N \approx 3$–4) is indicative of domains composed of few graphene layers, typical of hard carbons. The higher value shown for HCcom is consistent with the other parameters determined and further confirms a more extended aromatic system with respect to bio-HC.

Raman spectroscopy is useful to investigate the structural ordering of hard carbon materials. A typical HC spectrum exhibits two broad bands, the D band (≈1350 cm^{-1}) representative for the disordered region and the G band (≈1580 cm^{-1}) characteristic of the graphitic portion [43, 44]. The G band corresponds to the in-plane stretching vibration of sp^2-bonded carbon atoms in graphitic domains, while the D band arises from breathing modes of aromatic rings that become Raman-active due to structural defects and finite crystallite size. The integrated area ratio A(D)/A(G) is used as an indicative measure of the structural disorder: higher values indicate smaller graphitic domains and a higher defect density. The intensity ratio I(D)/I(G) was, instead, used to determine the average crystallite size (L_a), already described above in the XRD section. The obtained Raman spectra are shown in Figure 2c, while the full deconvolution of spectra, managed in the interval 800–1800 cm^{-1}, is shown in Figure S5. The resulting parameters are summarized in Table S5. The integrated area ratio A(D)/A(G) > 1, as well as the intensity ratio I(D)/I(G), is typical of disordered carbon materials. The three bio-HC exhibit high A(D)/A(G) ratios (>3), indicative of highly disordered structures typical of non-graphitizable carbons. Among the three samples, OLV shows the highest ratio (4.10), suggesting the greatest defect density and the lowest degree of aromatic ordering. HZN displays an intermediate value (3.83), reflecting a slightly higher organization of sp^2 micro-domains, while CAN exhibits the lowest ratio (3.44), indicating a relatively more coherent arrangement of aromatic domains. The commercial HC resulted in a ratio comparable to CAN. In terms of I(D)/I(G), again a trend is observed with the order HCcom < HZN < CAN < OLV, confirming CAN and OLV as the most defective in the set. The values of La obtained from Raman spectrum deconvolution (Table S5) are compared with the ones obtained from the deconvolution of the diffractograms (Table S4). Raman and XRD provide complementary insights into the structural order of the HCs by probing different length scales. Raman spectroscopy is highly sensitive to local defects, with the D-band signal originating from disordered regions and edges, resulting in smaller calculated domain sizes (L_a) that reflect local aromatic coherence. In contrast, XRD averages over larger volumes, detecting only sufficiently ordered crystallites and thus often reporting larger domain sizes. Therefore, the same sample can appear more disordered by Raman spectroscopy than by XRD due to their varying sensitivities to different structural features. Based on such assumptions, the following trend is observed: HCcom < HZN < CAN < OLV. The results obtained from Raman seem to show an opposite tendency respect to the ones obtained with XRD, because Raman is highly sensitive to local defects and the effective size of ordered sp^2 domains. HCcom exhibits a larger lateral extension of graphitic domains, as inferred from XRD, but exhibited a smaller L_a value from Raman spectroscopy, indicating a higher density of local structural defects within the aromatic planes. Conversely, the bio-HC show smaller graphitic domains according to XRD, yet a relatively larger L_a from Raman, indicating fewer local defects and a more homogeneous short-range structure.

Lastly, the analysis of the surface chemistry of the samples was performed with XPS to evaluate the presence of contaminants, already identified in the bulk using EDX. The comparison of the XPS surveys of the bio-HC and HCcom is reported in Figure 2d. As can be seen, the surface is composed predominantly of C and O in different amounts, with the presence of Si as contaminant in CAN. The elemental composition (Table S6) resulted in contents higher than 93 at.% of C, with HZN possessing the highest amount of O (~7 at.%). The OLV and HCcom compositions resulted very similar, while CAN is characterized by the presence of 1 at.% of Si. The full deconvolution of the identified core levels is performed according to the literature of electroactive carbonaceous material (C1s, O1s) [45–54] and to specific Si containing carbon materials (Si2p) [55–59]. The results are reported in Figures S6–S8 and summarized in Table S7. In the C1s, the main component identified is graphitic carbon (Csp^2) at the binding energy (BE) of 284.5 eV [60–62] with a content higher than 60 rel.% with OLV and Hccom reaching 70 rel.%. The second C moiety identified is disordered sp^3 C (285.5–286 eV) [63–65] with a maximum of 9.6 rel.% for CAN. Four different O-containing groups are also present in the BE range 286–290 eV [63–65]. Interestingly, HZN possessed the highest amount of C—OH (12.1 rel.%) compared to *ca* half the amount in the other samples. Such functional groups have been previously associated with irreversible capacity in HC anodes for SIB [66, 67]. The remaining groups accounted for less than 15 rel.% for all the samples.

Lastly, regarding the CAN sample, the contaminant identified is consistent with an oxidized form of Si, (SiOx, 103.6 eV).

As a final step of the bio-HC characterization, a full electrochemical analysis is performed to investigate the electrochemical Na^+ ions storage capability in terms of specific capacity. The electrodes were prepared using the 85:10:5 ratio of active material, conductive carbon (SuperP) and carboxymethyl cellulose (CMC) in water. The galvanostatic cycling (GC) was performed at a current density of 10 mA g^{-1} for at least 10 cycles, and the corresponding results are shown in Figure 3. The sodium storage capacity in HC is known to be influenced by the type of biomass used as precursor [68]. All the bio-derived HCs analyzed exhibit good electrochemical performance, summarized in Table S8. The most evident feature in the GC curves is the difference in the sodium storage reaction mechanism with different SEI formation. The HCcom displays a pronounced plateau of ≈100 mAh g^{-1} at around 0.1 V vs Na^+/Na, followed by a monotonic voltage rise up to the upper cut-off limit. In contrast, all bio-based samples show, beyond the first plateau, an inflection point near 0.6 V vs Na^+/Na, leading to a secondary pseudo-plateau (see Plateau 2 in Table S8), as already observed in the literature [29]. The capacity contribution in this region increases progressively from sample HZN to CAN and OLV. The higher the capacity in this low-voltage region, the better the overall electrochemical performance. From the capacity vs. cycle number plot (Figure S9), the reversible capacity of each sample can be extracted. HZN exhibits the lowest reversible capacity (220 mAh g^{-1}), eventually due to the higher content of C—O/C—OH groups evidenced from XPS, followed by both the commercial HC and CAN (270 mAh g^{-1}). The highest reversible capacity, 290 mAh g^{-1}, is achieved by OLV. Both CAN and OLV are characterized by a higher interlayer spacing capable of better accommodating Na^+ ions, as observed in the XRD section. The capacity loss after the first discharge, reported as a percentage in Table S8, corresponds to the initial Coulombic efficiency (ICE). A low ICE indicates high irreversibility, typically associated with the formation of an SEI. In the GC curves, this first-cycle irreversibility can be identified by a larger ohmic drop between the first and second discharge. This effect is particularly evident in HZN, which shows the lowest ICE (55%). The ICE increases from CAN (67%) to OLV (76%) and HCcom (77%). To contextualize the results, a summary of existing literature of biowaste-based HC for SIB anodes is reported in Table 1.

The best-performing bio-based samples, CAN and OLV, were further compared under increasing C-rates following initial cell activation, testing at C/10, C/5, C/2, 1C, and 2C, followed by 100 cycles at 1C. This high current rate comparison is shown in Figure S10. During the test, OLV remained the best performing sample, although the performance gap with CAN narrowed as the rate increased. At 1C, OLV retained a capacity of 90 mAh g^{-1}, compared to 75 mAh g^{-1} for CAN. Doubling the current to 2C reduced the difference to only 10 mAh g^{-1} (OLV: 65 mAh g^{-1}; CAN: 55 mAh g^{-1}). After 100 cycles, however, the capacity of CAN (40 mAh g^{-1}) slightly exceeded that of OLV (33 mAh g^{-1}), likely due to a gradual loss of the low-voltage plateau, which shifted below the cut-off potential of 0.01 V vs Na^+/Na for all the HC samples [75]. The observed long-term capacity fade arises from coupled structural and chemical evolution revealed by XPS and SAXS. XPS indicates progressive growth and chemical changes in the surface film—consistent with repeated SEI rupture/reformation and ongoing electrolyte decomposition—which consume cyclable Na and increase interfacial resistance. SAXS reveals a reduction and reorganization of open porosity consistent with pore narrowing, partial pore filling, or structural collapse during cycling. These changes reduce accessible low-energy insertion and pore-filling sites and promote irreversible Na trapping and clustering, directly

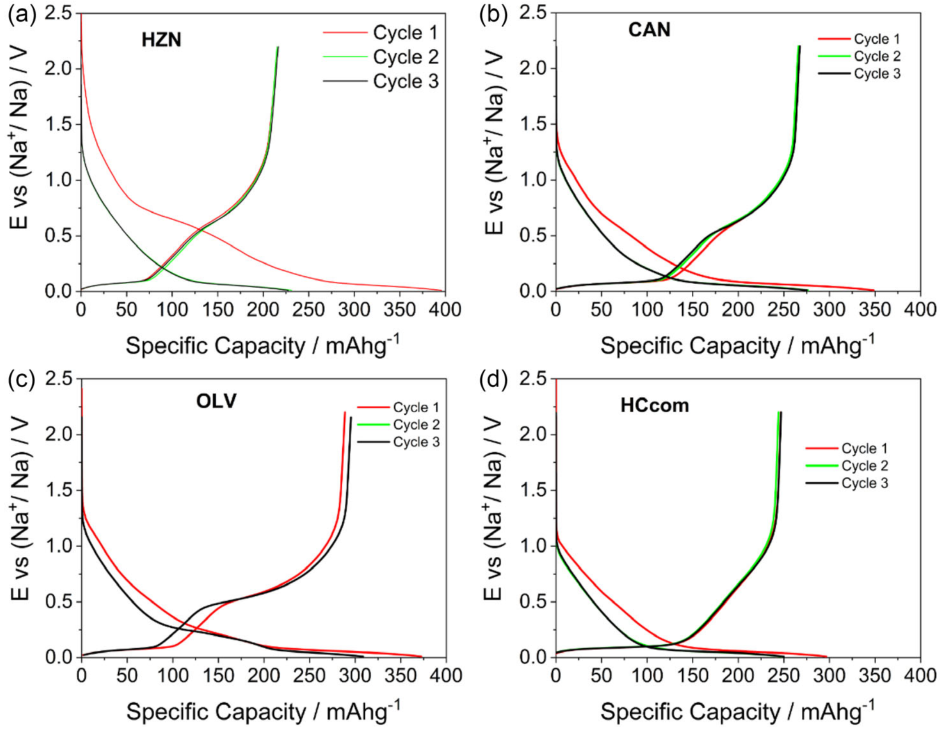

FIGURE 3 | Galvanostatic charge/discharge cycles of Na(0)| EC + PC, $NaClO_4$|HC half cells at a current density of 10 mA g^{-1} for 10 cycles. (a) HZN, (b) CAN, (c) OLV, (d) HCcom.

TABLE 1 | Comparison of synthesis procedure and electrochemical performance of biowaste-based HC for SIB anodes.

Biowaste precursor	Synthesis procedure	Thermal treatment (°C)	Reversible capacity (mAh g^{-1})	ICE (%)	Stability (cycles)	Ref.
Sugarcane bagasse	Pre and post pyrolysis washing in H_2O and ethanol	950, 6 h	212 (0.05 Ag^{-1})	n.d.	300	[20]
Vine shoots	pre-pyrolysis at 500°C + HCl washing	1200, 2 h	259 (0.03 Ag^{-1})	71	315	[21]
Wheat straw	Autoclave, NaOH, 180°C, 6 h. Washing, HCl, 80°C, 2 h.	700, 2 h	322 (0.2C)	39	300	[24]
Peanut Shells	Post-pyrolysis washing with 10% KOH, 2 h then HCl, 2 h.	800, 2 h	320 (0.1 Ag^{-1})	n.d.	500	[28]
Green Peas Pod	pre-pyrolysis at 500°C, 5 h + 6 M H_3PO_4 washing	1400, 2 h	293 (0.1C)	74	100	[29]
Sisal fiber	Autoclave, KOH, 160°C, 14 h	900, 1 h	265 (0.1 Ag^{-1})	77	400	[69]
Aegle marmelos shell	Autoclave, H_2SO_4, 200°C, 48 h	900, 1000	223 (900°C), 212 (1000°C) (0.01Ag^{-1})	99	2500	[70]
Pomegranate peel	Acid washing with HCl and HF	1100, 2 h	330 (0.1C)	45	200	[71]
Spent coffee grounds	Autoclave, water, 250°C, 24 h	1200, 2 h	240 (C/15)	40	500	[72]
Walnut shell + polystyrene	Pre-carbonization at 1000°C + 700°C + polystyrene	1200, 2 h	385 (0.05 Ag^{-1})	88	300	[73]
Lignin	none	1500, 1 h	27 (0.04 Ag^{-1})	80	50	[74]
Chitosan	none	1500, 1 h	25 (0.04 Ag^{-1})	86	50	[74]
Olive Stones	Autoclave 5% citric acid, 200°C, 14 h	1100, 2 h	290 (0.01 Ag^{-1})	76	100	This work

accounting for the attenuation and disappearance of the low-voltage plateau (linked to Na insertion into graphitic-like domains, pore filling, and clustering) [76]. Diffusion limitations at the applied 1C rate, together with increased transport impedance from a thicker, less-permeable SEI, further restrict utilization of remaining sites. Collectively, these structural and chemical evolutions explain the irreversible capacity loss and the specific suppression of the low-voltage plateau during long-term cycling.

Summarizing, the electrochemical trends observed are peculiar to the precursors used for the synthesis, especially in terms of SEI formation and reversible specific capacity. CAN and OLV resulted in the best bio-HC in terms of morphology, pore size, interlayer spacing, defectivity, and surface chemistry, directly observed with thinner SEI and higher ICE. Further investigations are required to thoroughly characterize the peculiar behavior observed upon GC cycling, in order to understand how to progressively improve storage capability.

3 | Conclusions

The replacement of CRM and unsustainable precursors for the synthesis of electroactive materials is nowadays a hot topic needing attention. The possibility of using waste biomasses for the preparation of anode materials for SIB could overcome the requirements of sustainability of the outcoming Circular Economy Act of the EU. This work highlights the potential of tailored microstructural design in biomass-derived hard carbons for sodium-ion batteries. By employing a controlled synthesis process involving ball milling, citric acid digestion, and pyrolysis, we obtained HCs from Italian waste biomasses with specific surface areas and interlayer spacings conducive to sodium-ion insertion/adsorption. These materials exhibited electrochemical performance on par with commercial hard carbon, demonstrating that the unique combination of properties arising from the biowaste precursors can be harnessed for effective energy storage. Our results emphasize the importance of understanding and controlling the microstructure-performance relationship in sustainable anode materials to drive advancements in sodium-ion battery technology.

4 | Methods

4.1 | Material Synthesis

The three samples used in this study were synthesized using Italian biowaste resources available on the territory. Specifically, Tonda Gentile Romana variety hazelnut shell (labeled as HZN), Arundo donax variety wild giant cane (labeled as CAN), and mixed variety fragmented olive stone (labeled as OLV). The synthesis protocol required a 30-minute ball milling divided in two rounds with 15 min rest between rounds using a SPEX Sample Prep 8000 M Mixer/Mill with 0.8 mm stainless steel spheres and a ratio of 1:6, precursor-to-spheres, followed by a 5 wt.% citric acid (Sigma–Aldrich anhydrous, ACS reagent grade) digestion with 1:2.5 in mass of precursor to water ratio in autoclave at 200°C for 14 h. After that, a washing and vacuum-filtration process until neutral pH followed by 20 h muffle furnace drying at 60°C. Lastly, a pyrolysis step performed at 1100°C for 2 h, 5°C min^{-1}, under 50 mL min^{-1} Ar/H_2 (Sapio Hydroplus 5 mix, H_2 5%) continuous flux until room temperature.

To compare the results obtained, a commercial Hard Carbon was used without further modifications and labeled as HCcom. The reference material is Carbotron P sold by Kureha battery Materials Japan Co., Ltd.

4.2 | Material Characterization

4.2.1 | Scanning Electron Microscopy and Energy-Dispersive X-Ray Spectroscopy

A field emission scanning electron microscope (FE-SEM) Leo SUPRA 35, Carl Zeiss was employed for morphological investigations. Samples were observed without prior conductive layer sputtering. EDX analyses were carried out using a 20 kV accelerating voltage. Emitted X-rays were collected using a Ultim Max "Infinity" SDD 170 mm^2 detector by Oxford Instruments. At least three different areas were considered for each sample (each area ~0.08 mm^2).

4.2.2 | Raman Spectroscopy

Raman analysis was performed with a micro-Raman spectrophotometer (DilorLabram, Horiba Jobin Yvon, Edison, USA), 632 nm excitation wavelength, Peltier CCD camera detector, 1800 gr mm^{-1} grating, and edge filter with a cut-off at 150 cm^{-1}.

The Raman spectra were fitted using the software fityk. To determine the average crystallite size (La) from amorphous carbon, Ferrari and Robertson (Equation (1)) modified Tuinstra and Koenig equation that is valid for ordered graphitic carbons and obtained [77, 78]:

$$L_a = \sqrt{\frac{\mathrm{I(D)}}{\mathrm{I(G)}} \cdot \frac{1}{\mathrm{C}(\lambda_\mathrm{L})}} \tag{1}$$

in which $\mathrm{C}(\lambda_\mathrm{L})$ was experimental calculated and it is equal to $\mathrm{C}(\lambda_\mathrm{L}) \approx \mathrm{C}_0 + \lambda_\mathrm{L}\mathrm{C}_1$, with $\mathrm{C}_0 = -12.6$ nm and $\mathrm{C}_1 = 0.033$, valid for 400 nm $< \lambda_\mathrm{L} <$ 700 nm, in our case $\lambda_\mathrm{L} = 623$ nm.

4.2.3 | X-Ray Diffraction

X-ray diffraction analysis was carried out on HC powders (diffractometer SmartLab Rigaku), Cu-Kα λ = 1.54 Å, 40 kV, 30 mA. The signal was collected in the range of 2θ: 10°–90° with a step of 0.02° and a scan rate of 0.4° min. The diffractograms obtained were fitted using the software OctCarb [42].

The main structural parameters derived are:

- $\mathrm{L_a}$ = average graphene layer size
- $\mathrm{L_c}$ = average stack height
- N = average number of graphene layers per stack
- $\mathrm{l_m}$ = average chord length
- $\mathrm{a_3}$ = average layer distance
- lcc = average C—C bond length

4.2.4 | SAXS

SAXS measurements were performed at SAXSLab Sapienza with a Xeuss 2.0 Q-Xoom system (Xenocs SAS, Grenoble, France), equipped with a micro-focus Genix 3D X-ray source with Cu anode (λ = 0.1542 nm) a two-dimensional Pilatus3 R 300 K detector, which can be placed at variable distance from the sample and an additional Pilatus3 R 100 K detector at fixed shorter distance from the sample (around 14 cm) and tilted at 36° to access larger scattering angles (Dectris Ltd., Baden, Switzerland). Calibration of the sample-detector distance was performed using silver behenate for the small-angle region and Al_2O_3 for the fixed-distance wide-angle detector. The beam size was defined to be 0.5 mm × 0.5 mm through the two-pinhole collimation system equipped with "scatterless" slits. Measurements with two sample-to-detector distances (262 and 2500 mm) were performed so that the overall explored range of the scattering vector modulus q ($q = 4\pi\sin\theta/\lambda$ with 2θ the scattering angle and λ the photon wavelength) was 0.04 $\text{nm}^{-1} < q < 32$ nm^{-1}. The powders were loaded within 1-mm thick washers with adhesive Kapton windows and measured in the instrument sample chamber at reduced pressure (~0.2 mbar) at room temperature (23°C–25°C). The two-dimensional scattering patterns collected with a total acquisition time of 0.5 h per sample were automatically corrected for cosmic radiation features and subtracted for the "dark" counts, and then masked, azimuthally averaged, and normalized for transmitted beam intensity, exposure time and subtended solid angle per pixel, using the FOXTROT software developed at SOLEIL. The one-dimensional intensity vs. q profiles were then subtracted for the data of the empty Kapton windows, and the three angular ranges were merged using the tool of SAXSutilities2 [79]. The final data were normalized by the sample thickness of 0.1 cm to obtain intensity in cm^{-1} units (macroscopic scattering cross section).

4.2.5 | XPS

The X-ray photoelectron spectroscopy (XPS) analysis was performed in ultrahigh vacuum (UHV, <10^{-10} mBar) using a SPECS PHOIBOS 150 XPS system equipped with monochromatic Al Kα (1486.6 eV) X-ray source and high-speed imaging 2D CMOS true counting detector. The system was calibrated using the Au4f spectrum at 84 eV. The samples were prepared over a stainless-steel custom made multisample holder. The full survey and C1s, O1s, Na1s, and Si2p core levels were recorded for each sample. The passing energy was set to 20 eV. The fittings were performed using Kalibri KolXPD software.

4.3 | Electrochemical Testing

The HC anodes were prepared by mixing the active materials with super P (as conducting material), carboxymethylcellulose

(CMC) solution in water (as binder) in a weight ratio of 85:10:5 to obtain the slurry mixture. The slurry was spread on aluminum foil by using a doctor blade set at 200 µm thickness. Hereafter, the aluminum-coated foil was dried in an oven at RT for around 3 h and cut into a round electrode of 10 mm diameter. The electrodes were dried overnight into a Büchi oven at 170°C under vacuum for 24 h, then transferred into an Ar-filled glove box (Jacomex GP-Concept) to assemble cells (coin cells 2032) in an inert atmosphere (H_2O, $O_2 < 1$ ppm).

HCs electrochemical performances have been investigated in half cells set up with a sodium metal as counter electrode. Whatman glass fiber disks were used as separators soaked with 100 µL of electrolyte solution composed of $NaClO_4$ 1 M in a mixture of ethylene carbonate (EC) and propylene carbonate (PC) in a weight ratio EC:PC = 1:1.

The cells were electrochemically tested by galvanostatic cycling (CG) at 10 mA g^{-1} and then using different C-rates (C/30, C/10, C/5, C/2, 1C, 2C with 1C = 300 mAh/g). After that, 100 cycles at 1C are performed. For the tests, a cutoff voltage between 10 mV and 2.2 V was used.

The extrapolated data are obtained from three different tests, averaged and reported in standard deviation.

Acknowledgments

The XPS experiments were carried out at the SmartLab departmental laboratory of the Department of Physics at Sapienza University of Rome. V.C.A.F. and E.P. acknowledge Dr. Marco Sbroscia for his assistance during the measurements. The Sapienza Research Infrastructure is acknowledged for the SAXS measurements at SAXSLab Sapienza, funded by the Large Equipment Project 2015-C26J15BX54.

Open access publishing facilitated by ENEA Agenzia Nazionale per Le Nuove Tecnologie l'Energia e lo Sviluppo Economico Sostenibile, as part of the Wiley - CRUI-CARE agreement.

Funding

S.B. would like to thank the Hymetbat project funded under the framework of the (24GRD09) call (European Partnership on Metrology). C.P. acknowledges the financial support of Ministry of Environment and Energy Security for funding Project 1.2 (Integrated project on electrochemical and thermal storage technologies) CUP: (I53C24003300001) in the framework of "Ricerca di Sistema Elettrico"—(PTR 25-27). G.G acknowledges the European Union's Horizon 2020 research and innovation program under the Marie Sklodowska-Curie (101029608).

Conflicts of Interest

The authors declare no conflicts of interest.

Data Availability Statement

Data available on request.

References

1. European Commission, *Circular Economy Action Plan: For a Cleaner and More Competitive Europe* (Luxembourg: Publications Office of the European Union, 2020, https://data.europa.eu/doi/10.2779/05068.

2. M. Okoshi, Y. Yamada, S. Komaba, A. Yamada, and H. Nakai, "Theoretical Analysis of Interactions between Potassium Ions and Organic Electrolyte Solvents: A Comparison with Lithium, Sodium, and Magnesium Ions," *Journal of the Electrochemical Society* 164, no. 2 (2016): A54, https://doi.org/10.1149/2.0211702jes.

3. N. Yabuuchi, K. Kubota, M. Dahbi, and S. Komaba, "Research Development on Sodium-Ion Batteries," *Chemical Reviews* 114, no. 23 (2014): 11636–11682, https://doi.org/10.1021/cr500192f.

4. Jean-Marie Tarascon, "Na-Ion versus Li-Ion Batteries: Complementarity Rather than Competitiveness," *Joule* 4, no. 8 (2020): 1616–1620, https://doi.org/10.1016/j.joule.2020.06.003.

5. D. Alvira, D. Antorán, and J. J. Manyà, "Plant-Derived Hard Carbon as Anode for Sodium-Ion Batteries: A Comprehensive Review to Guide Interdisciplinary Research," *Chemical Engineering Journal* 447 (2022): 137468, https://doi.org/10.1016/j.cej.2022.137468.

6. M. Liu, Y. Wang, F. Wu, et al., "Advances in Carbon Materials for Sodium and Potassium Storage," *Advanced Functional Materials* 32, no. 31 (2022): 2203117, https://doi.org/10.1002/adfm.202203117.

7. C. A. T. L. n.d, "Naxtra Battery Breakthrough & Dual-Power Architecture: CATL Pioneers the Multi-Power Era," (2025), https://www.catl.com/en/news/6401.html.

8. L. Sun, J. Zeng, X. Wan, et al., "Recent Progress of Interface Modification of Layered Oxide Cathode Material for Sodium-Ion Batteries," *EScience* 2 (2024): e31, https://doi.org/10.1002/elt2.31.

9. X. Wei, W. Wu, H. Liu, et al., "An Overview of the Modification Strategies for P2-Na2/3Ni1/3Mn2/3O2 Cathode for Sodium-Ion Batteries," *Sustainable Materials and Technologies* 41 (2024): e01059, https://doi.org/10.1016/j.susmat.2024.e01059.

10. Y. Huang, W. Mu, X. Bi, et al., "Progress in Defect Engineering of High-Performance Prussian Blue Analogues as Cathode Materials for Sodium-Ion Batteries," *Journal of Energy Storage* 111 (2025): 115435, https://doi.org/10.1016/j.est.2025.115435.

11. Y. Dou, L. Zhao, Y. Liu, et al., "High-Abundance and Low-Cost Anodes for Sodium-Ion Batteries," *Carbon Neutralization* 3 (2024): 954–995, https://doi.org/10.1002/cnl2.171.

12. D. P. DiVincenzo and E. J. Mele, "Cohesion and Structure in Stage-1 Graphite Intercalation Compounds," *Physical Review B* 32, no. 4 (1985): 2538–2553, https://doi.org/10.1103/PhysRevB.32.2538.

13. O. Lenchuk, P. Adelhelm, and D. Mollenhauer, "New Insights into the Origin of Unstable Sodium Graphite Intercalation Compounds," *Physical Chemistry Chemical Physics* 21 (2019): 19378–19390, https://doi.org/10.1039/C9CP03453F.

14. D. A. Stevens and J. R. Dahn, "High Capacity Anode Materials for Rechargeable Sodium-Ion Batteries," *Journal of the Electrochemical Society* 147, no. 4 (2000): 1271, https://doi.org/10.1149/1.1393348.

15. Y. Cao, L. Xiao, M. L. Sushko, et al., "Sodium Ion Insertion in Hollow Carbon Nanowires for Battery Applications," *Nano Letters* 12, no. 7 (2012): 3783–3787, https://doi.org/10.1021/nl3016957.

16. C. Bommier, T. W. Surta, M. Dolgos, and X. Ji, "New Mechanistic Insights on Na-Ion Storage in Nongraphitizable Carbon," *Nano Letters* 15, no. 9 (2015): 5888–5892, https://doi.org/10.1021/acs.nanolett.5b01969.

17. S. Alvin, D. Yoon, C. Chandra, et al., "Revealing Sodium Ion Storage Mechanism in Hard Carbon," *Carbon* 145 (2019): 67–81, https://doi.org/10.1016/j.carbon.2018.12.112.

18. N. Sun, Z. Guan, Y. Liu, et al., "Extended Adsorption–Insertion Model: A New Insight into the Sodium Storage Mechanism of Hard Carbons," *Advanced Energy Materials* 9, no. 32 (2019): 1901351, https://doi.org/10.1002/aenm.201901351.

19. X. Dou, I. Hasa, D. Saurel, et al., "Hard Carbons for Sodium-Ion Batteries: Structure, Analysis, Sustainability, and Electrochemistry," *Materials Today* 23 (2019): 87–104, https://doi.org/10.1016/j.mattod.2018.12.040.

20. S. A. Hashmi. Mohit, "Hard Carbon Anode Derived from Pre-Treated Bio-Waste Sugarcane Bagasse for High Capacity Sodium-Ion Battery

Fabricated with Biodegradable Porous Polymer Electrolyte," *Journal of Energy Storage* 83 (2024): 110694, https://doi.org/10.1016/j.est.2024.110694.

21. D. Alvira, D. Antorán, M. Vidal, V. Sebastian, and J. J. Manyà, "Vine Shoots-Derived Hard Carbons as Anodes for Sodium-Ion Batteries: Role of Annealing Temperature in Regulating Their Structure and Morphology," *Batteries & Supercaps* 6 (2023): e202300233, https://doi.org/10.1002/batt.202300233.

22. M. Wahid, Y. Gawli, D. Puthusseri, A. Kumar, M. V. Shelke, and S. Ogale, "Nutty Carbon: Morphology Replicating Hard Carbon from Walnut Shell for Na Ion Battery Anode," *ACS Omega* 2, no. 7 (2017): 3601–3609, https://doi.org/10.1021/acsomega.7b00633.

23. H. Moon, A. Innocenti, H. Liu, et al., "Bio-Waste-Derived Hard Carbon Anodes Through a Sustainable and Cost-Effective Synthesis Process for Sodium-Ion Batteries," *ChemSusChem* 16 (2023): e202201713, https://doi.org/10.1002/cssc.202201713.

24. P. Wang, H. Wang, C. Liang, and K. Yu, "Two-Dimensional Porous Flake Biomass Carbon with Large Layer Spacing as an Anode Material for Sodium Ion Batteries," *Diamond and Related Materials* 131 (2023): 109601, https://doi.org/10.1016/j.diamond.2022.109601.

25. T. Xu, X. Qiu, X. Zhang, and Y. Xia, "Regulation of Surface Oxygen Functional Groups and Pore Structure of Bamboo-Derived Hard Carbon for Enhanced Sodium Storage Performance," *Chemical Engineering Journal* 452 (2023): 139514, https://doi.org/10.1016/j.cej.2022.139514.

26. U. Kumar, J. Wu, N. Sharma, and V. Sahajwalla, "Biomass Derived High Areal and Specific Capacity Hard Carbon Anodes for Sodium-Ion Batteries," *Energy & Fuels* 35, no. 2 (2021): 1820–1830, https://doi.org/10.1021/acs.energyfuels.0c03741.

27. J. Liao, H. Qiu, P. Zhou, et al., "Unraveling the Effect of the Microstructure of Agricultural Waste Plants-Derived Hard Carbons on the Sodium Storage Performance," *Fuel* 376 (2024): 132664, https://doi.org/10.1016/j.fuel.2024.132664.

28. K. Rajpura, Y. Patel, R. Patel, and I. Mukhopadhyay, "Peanut-Shell Derived Hard Carbon as Potential Negative Electrode Material for Sodium-Ion Battery," *Journal of Materials Science: Materials in Electronics* 35 (2024): 951, https://doi.org/10.1007/s10854-024-12696-0.

29. M. Venkatesh, P. L. Mani Kanta, T. Thomas, R. Vijay, T. N. Rao, and B. Das, "Green Peas Pod Derived Hierarchical Porous N-Doped Hard Carbon as High Performance Anode for Sodium Ion Battery," *Biomass and Bioenergy* 194 (2025): 107646, https://doi.org/10.1016/j.biombioe.2025.107646.

30. L. Bottoni, H. Darjazi, L. Sbrascini, et al., "Electrochemical Characterization of Charge Storage at Anodes for Sodium-Ion Batteries Based on Corncob Waste-Derived Hard Carbon and Binder," *ChemElectroChem* 10 (2023): e202201117, https://doi.org/10.1002/celc.202201117.

31. Y. Chen, F. Li, Z. Guo, et al., "Sustainable and Scalable Fabrication of High-Performance Hard Carbon Anode for Na-Ion Battery," *Journal of Power Sources* 557 (2023): 232534, https://doi.org/10.1016/j.jpowsour.2022.232534.

32. A. Sidana, S. Kaur, and S. K. Yadav, "Assessment of the Ability of, *Meyerozyma Guilliermondii*, P14 to Produce Second-Generation Bioethanol from Giant Reed (*Arundo Donax*) Biomass," *Biomass Conversion and Biorefinery* 13 (2023): 16723–16735, https://doi.org/10.1007/s13399-021-02211-4.

33. J. Zhao, X. Jin, M. Yan, C. Huang, Q. Yong, and Z. Ling, "Supramolecular Regulation and Controllable Coproduction of Bamboo Nanocellulose and Mono/Oligosaccharides via Dual-Enzymatic Treatment Assisted by Ball Milling," *ACS Sustainable Chemistry & Engineering* 12 (2024): 15216–15227, https://doi.org/10.1021/acssuschemeng.4c06144.

34. R. Ryoo, S. H. Joo, M. Kruk, and M. Jaroniec, "Ordered Mesoporous Carbons," *Advanced Materials* 13, no. 9 (2001): 677–681, https://doi.org/10.1002/1521-4095(200105)13:9<677::AID-ADMA677>3.0.CO;2-C.

35. B. Zhong, C. Liu, D. Xiong, et al., "Biomass-Derived Hard Carbon for Sodium-Ion Batteries: Basic Research and Industrial Application," *ACS Nano* 18 (2024): 16468–16488, https://doi.org/10.1021/acsnano.4c03484.

36. L. Kalder, A. Olgo, J. Lührs, et al., "Empirical Correlation of Quantified Hard Carbon Structural Parameters with Electrochemical Properties for Sodium-Ion Batteries Using a Combined WAXS and SANS Analysis," *Energy Storage Materials* 67 (2024): 103272, https://doi.org/10.1016/j.ensm.2024.103272.

37. N. Yoshizawa, *Progress in Structure Characterization of Porous Carbon Materials by XRD and TEM* (Tanso 2006), 25–30, 2006, https://doi.org/10.7209/tanso.2006.25.

38. T. Pfaff, F. M. Badaczewski, M. O. Loeh, et al., "Comparative Microstructural Analysis of Nongraphitic Carbons by Wide-Angle X-Ray and Neutron Scattering," *Journal of Physical Chemistry C* 123, no. 33 (2019): 20532–20546, https://doi.org/10.1021/acs.jpcc.9b03590.

39. K. Faber, F. Badaczewski, W. Ruland, and B. M. Smarsly, "Investigation of the Microstructure of Disordered, Non-Graphitic Carbons by an Advanced Analysis Method for Wide-Angle X-Ray Scattering," *Zeitschrift für Anorganische Und Allgemeine Chemie* 640 (2014): 3107–3117, https://doi.org/10.1002/zaac.201400210.

40. K. Faber, F. Badaczewski, M. Oschatz, et al., "In-Depth Investigation of the Carbon Microstructure of Silicon Carbide-Derived Carbons by Wide-Angle X-Ray Scattering," *Journal of Physical Chemistry C* 118, no. 29 (2014): 15705–15715, https://doi.org/10.1021/jp502832x.

41. W. Ruland and B. Smarsly, "X-Ray Scattering of Non-Graphitic Carbon: An Improved Method of Evaluation," *Journal of Applied Crystallography* 35 (2002): 624–633, https://doi.org/10.1107/S0021889802011007.

42. O. Osswald and B. M. Smarsly, "OctCarb—A GNU Octave Script for the Analysis and Evaluation of Wide-Angle Scattering Data of Non-Graphitic Carbons," *C* 8, no. 4 (2022): 78, https://doi.org/10.3390/c8040078.

43. F. Tuinstra and J. L. Koenig, "Raman Spectrum of Graphite," *Journal of Chemical Physics* 53, no. 3 (1970): 1126–1130, https://doi.org/10.1063/1.1674108.

44. A. C. Ferrari and J. Robertson, "Interpretation of Raman Spectra of Disordered and Amorphous Carbon," *Physical Review B* 61, no. 20 (2000): 14095–14107, https://doi.org/10.1103/PhysRevB.61.14095.

45. D. Briggs and G. Beamson, "XPS Studies of the Oxygen 1s and 2s Levels in a Wide Range of Functional Polymers," *Analytical Chemistry* 65 (1993): 1517–1736, https://doi.org/10.1021/ac00059a006.

46. A. A. Myint, H. W. Lee, B. Seo, et al., "One-Pot Synthesis of Environmentally Friendly Lignin Nanoparticles with Compressed Liquid Carbon Dioxide as an Antisolvent," *Green Chemistry* 18 (2016): 2129–2146, https://doi.org/10.1039/C5GC02398J.

47. B. Ricciardi, B. Mecheri, W. da Silva Freitas, et al., "Porous Iron–Nitrogen–Carbon Electrocatalysts for Anion Exchange Membrane Fuel Cells (AEMFC)," *ChemElectroChem* 10 (2023): e202201115, https://doi.org/10.1002/celc.202201115.

48. B. Ricciardi, W. da Silva Freitas, B. Mecheri, et al., "Hierarchical Porous Fe/Ni-Based Bifunctional Oxygen Electrocatalysts for Rechargeable Zinc-Air Batteries," *Carbon* 219 (2024): 118781, https://doi.org/10.1016/j.carbon.2023.118781.

49. W. da Silva Freitas, A. D'Epifanio, C. Lo Vecchio, et al., "Tailoring MOF Structure via Iron Decoration to Enhance ORR in Alkaline Polymer Electrolyte Membrane Fuel Cells," *Chemical Engineering Journal* 465 (2023): 142987, https://doi.org/10.1016/j.cej.2023.142987.

50. M. Rahimihaghighi, M. Gigli, V. C. A. Ficca, E. Placidi, M. Sgarzi, and C. Crestini, "Lignin-Derived Sustainable Nano-Platforms: A

Multifunctional Solution for an Efficient Dye Removal," *ChemSusChem* 17 (2024): e202400841, https://doi.org/10.1002/cssc.202400841.

51. G. Zuccante, M. Muhyuddin, V. C. A. Ficca, et al., "Transforming Cigarette Wastes into Oxygen Reduction Reaction Electrocatalyst: Does Each Component Behave Differently? An Experimental Evaluation," *ChemElectroChem* 11 (2024): e202300725, https://doi.org/10.1002/celc.202300725.

52. L. Mirizzi, E. Carena, C. Santoro, et al., "Many Lives of Cobalt Within Electrochemical Systems: From Waste Batteries to Efficient Hydrogen Evolution Reaction Electrocatalyst," *Materials for Renewable and Sustainable Energy* 14 (2025): 37, https://doi.org/10.1007/s40243-025-00312-y.

53. L. Mirizzi, M. Muhyuddin, C. L. Vecchio, et al., "Amorphous Nanostructured Ni–Fe Oxide as a Notably Active and Low-Cost Oxygen Evolution Reaction Electrocatalyst for Anion Exchange Membrane Water Electrolysis," *Industrial Chemistry & Materials* 3 (2025): 485–497, https://doi.org/10.1039/D5IM00008D.

54. C. Xu, D. Zhang, G. Ma, et al., "Pre-Carbonization Facilitates Closed Pore Formation in Asphalt-Derived Hard Carbon for High-Plateau-Capacity Sodium Storage," *Chemical Engineering Journal* 520 (2025): 166398, https://doi.org/10.1016/j.cej.2025.166398.

55. C. Nita, J. Fullenwarth, L. Monconduit, et al., "Eco-Friendly Synthesis of SiO_2 Nanoparticles Confined in Hard Carbon: A Promising Material with Unexpected Mechanism for Li-Ion Batteries," *Carbon* 143 (2019): 598–609, https://doi.org/10.1016/j.carbon.2018.11.069.

56. B. Guo, J. Shu, Z. Wang, et al., "Electrochemical Reduction of Nano-SiO_2 in Hard Carbon as Anode Material for Lithium Ion Batteries," *Electrochemistry Communications* 10, no. 12 (2008): 1876–1878, https://doi.org/10.1016/j.elecom.2008.09.032.

57. D. Lv, L. Yang, R. Song, et al., "A Hierarchical Porous Hard Carbon@Si@Soft Carbon Material for Advanced Lithium-Ion Batteries," *Journal of Colloid and Interface Science* 678 (2025): 336–342, https://doi.org/10.1016/j.jcis.2024.09.009.

58. S. Yi, Z. Yan, X. Li, et al., "Design of Phosphorus-Doped Porous Hard Carbon/Si Anode with Enhanced Li-Ion Kinetics for High-Energy and High-Power Li-Ion Batteries," *Chemical Engineering Journal* 473 (2023): 145161, https://doi.org/10.1016/j.cej.2023.145161.

59. D. D'Ubaldo, M. Sbroscia, V. C. A. Ficca, et al., "Study of Defects Population and Contaminations in Silica/Tantala Coated Mirrors," *Journal of Vacuum Science & Technology B* 42 (2024): 034003, https://doi.org/10.1116/6.0003510.

60. B. Mecheri, V. C. A. Ficca, M. A. Costa de Oliveira, et al., "Facile Synthesis of Graphene-Phthalocyanine Composites as Oxygen Reduction Electrocatalysts in Microbial Fuel Cells," *Applied Catalysis B: Environmental* 237 (2018): 699–707.

61. V. C. A. Ficca, M. Sbroscia, E. Stellino, et al., "Non-Chemical Route to PGM-Free via N^+ Ion Implantation in Vertically Aligned Carbon Nanotubes," *Advanced Functional Materials* 35 (2025): 2413308, https://doi.org/10.1002/adfm.202413308.

62. L. Sallaku, L. Mirizzi, M. Muhyuddin, et al., "Upgrading the Waste Acrylonitrile-Butadiene-Styrene into Crude Oil and Highly Efficient Electrocatalysts for Oxygen Reduction Reaction," *Chemical Engineering Journal* 512 (2025): 162236, https://doi.org/10.1016/j.cej.2025.162236.

63. V. C. A. Ficca, C. Santoro, E. Placidi, et al., "Exchange Current Density as an Effective Descriptor of Poisoning of Active Sites in Platinum Group Metal-Free Electrocatalysts for Oxygen Reduction Reaction," *ACS Catalysis* 13 (2023): 2162–2175, https://doi.org/10.1021/acscatal.2c05222.

64. W. da Silva Freitas, B. Mecheri, C. Lo Vecchio, et al., "Metal-Organic-Framework-Derived Electrocatalysts for Alkaline Polymer Electrolyte Fuel Cells," *Journal of Power Sources* 550 (2022): 232135, https://doi.org/10.1016/j.jpowsour.2022.232135.

65. W. da Silva Freitas, A. D'Epifanio, V. C. A. Ficca, E. Placidi, F. Arciprete, and B. Mecheri, "Tailoring Active Sites of Iron–Nitrogen–Carbon Catalysts for Oxygen Reduction in Alkaline Environment: Effect of Nitrogen-Based Organic Precursor and Pyrolysis Atmosphere," *Electrochimica Acta* 391 (2021): 138899, https://doi.org/10.1016/j.electacta.2021.138899.

66. C. Chen, Y. Huang, Y. Zhu, et al., "Nonignorable Influence of Oxygen in Hard Carbon for Sodium Ion Storage," *ACS Sustainable Chemistry & Engineering* 8 (2020): 1497–1506, https://doi.org/10.1021/acssuschemeng.9b05948.

67. W. Shao, F. Hu, T. Zhang, et al., "Engineering Ultramicroporous Carbon with Abundant C═O as Extended Slope-Dominated Sodium Ion Battery Anodes," *ACS Sustainable Chemistry & Engineering* 9 (2021): 9727–9739, https://doi.org/10.1021/acssuschemeng.1c01885.

68. X.-X. He, L. Li, X. Wu, and S.-L. Chou, "Sustainable Hard Carbon for Sodium-Ion Batteries: Precursor Design and Scalable Production Roadmaps," *Advanced Materials* 37 (2025): 2506066, https://doi.org/10.1002/adma.202506066.

69. Y. Luo, Y. Xu, X. Li, K. Zhang, Q. Pang, and A. Qin, "Boosting the Initial Coulomb Efficiency of Sisal Fiber-Derived Carbon Anode for Sodium Ion Batteries by Microstructure Controlling," *Nanomaterials* 13 (2023): 881, https://doi.org/10.3390/nano13050881.

70. A. Patel, R. Mishra, R. K. Tiwari, et al., "Sustainable and Efficient Energy Storage: A Sodium Ion Battery Anode from Aegle Marmelos Shell Biowaste," *Journal of Energy Storage* 72 (2023): 108424, https://doi.org/10.1016/j.est.2023.108424.

71. Q. Wu, K. Shu, L. Zhao, and J. Zhang, "Pomegranate Peel-Derived Hard Carbons as Anode Materials for Sodium-Ion Batteries," *Molecules (basel, Switzerland)* 29 (2024): 4639, https://doi.org/10.3390/molecules29194639.

72. N. Nieto, J. Porte, D. Saurel, et al., "Use of Hydrothermal Carbonization to Improve the Performance of Biowaste-Derived Hard Carbons in Sodium Ion-Batteries," *ChemSusChem* 16 (2023): e202301053, https://doi.org/10.1002/cssc.202301053.

73. W. Li, J. Li, B. W. Biney, et al., "Innovative Synthesis and Sodium Storage Enhancement of Closed-Pore Hard Carbon for Sodium-Ion Batteries," *Energy Storage Materials* 74 (2025): 103867, https://doi.org/10.1016/j.ensm.2024.103867.

74. A. M. Escamilla-Pérez, A. Beda, L. Simonin, M.-L. Grapotte, J. M. Le-Meins, and C. Matei Ghimbeu, "Biopolymer-Based Hard Carbons: Correlations between Properties and Performance as a Na-Ion Battery Anode," *ACS Applied Energy Materials* 6 (2023): 7419–7432, https://doi.org/10.1021/acsaem.3c00640.

75. L. Wu, D. Buchholz, C. Vaalma, G. A. Giffin, and S. Passerini, "Apple-Biowaste-Derived Hard Carbon as a Powerful Anode Material for Na-Ion Batteries," *ChemElectroChem* 3 (2016): 292–298, https://doi.org/10.1002/celc.201500437.

76. N. Sun, J. Qiu, and B. Xu, "Understanding of Sodium Storage Mechanism in Hard Carbons: Ongoing Development Under Debate," *Advanced Energy Materials* 12 (2022): 2200715, https://doi.org/10.1002/aenm.202200715.

77. L. G. Cançado, K. Takai, T. Enoki, et al., "General Equation for the Determination of the Crystallite Size La of Nanographite by Raman Spectroscopy," *Applied Physics Letters* 88 (2006): 163106, https://doi.org/10.1063/1.2196057.

78. G. A. Zickler, B. Smarsly, N. Gierlinger, H. Peterlik, and O. Paris, "A Reconsideration of the Relationship between the Crystallite Size La of Carbons Determined by X-Ray Diffraction and Raman Spectroscopy," *Carbon* 44 (2006): 3239–3246, https://doi.org/10.1016/j.carbon.2006.06.029.

79. S. Michael, “*SAXSutilities2: A Graphical User Interface for Processing and Analysis of Small-Angle X-Ray Scattering Data*, 2021, ver 1.024, https://doi.org/10.5281/zenodo.5825707.

Supporting Information

Additional supporting information can be found online in the Supporting Information section. The supporting information is attached. **Supporting Fig. S1**. SEM micrographs at different magnifications of the ball milled bio-HC precursors: (a–b) HZN, (c–d) CAN, (e–f) OLV. Dimensions: a-c-e 10 μm, b-d-f 1 μm. **Supporting Fig. S2**. SEM micrographs at different magnifications of the autoclave digested bio-HC precursors: (a–b) HZN, (c–d) CAN, (e–f) OLV. Dimensions: a-c-e 10 μm, b-d-f 1 μm. **Supporting Fig. S3**. Krakty plot of the SAXS profiles of the prepared samples and commercial HC. **Supporting Fig. S4**. Full deconvolution of the XRD spectra of the prepared samples. (a) HZN, (b) CAN, (c) OLV, (d) HCcom. **Supporting Fig. S5**. Deconvolution of the Raman spectra of the samples. (a) HZN, (b) CAN, (c) OLV, (d) HCcom. **Supporting Fig. S6**. Full deconvolution of the C1s core levels of the prepared samples. (a) HZN, (b) CAN, (c) OLV, (d) HCcom. **Supporting Fig. S7**. Full deconvolution of the O1s core levels of the prepared samples. (a) HZN, (b) CAN, (c) OLV, (d) HCcom. **Supporting Fig. S8**. Full deconvolution of the Si2p core level of the CAN sample. **Supporting Fig. S9**. Specific capacity and coulombic efficiency (CE) vs cycles comparison (a) HZN, (b) CAN, (c) OLV, (d) HCcom. **Supporting Fig. S10**. C-Rate comparison between the sample (a) CAN, (b) OLV. **Supporting Table S1**. Elemental composition (wt%) of the ball milled precursors obtained via EDX analysis. 1wt% uncertainty is to be considered for all reported data. **Supporting Table S2**. Elemental composition (wt%) of the digested precursors obtained via EDX analysis. 1wt% uncertainty is to be considered for all reported data. **Supporting Table S3**. Elemental composition (wt%) of the pyrolyzed samples and commercial HC obtained via EDX analysis. 1wt% uncertainty is to be considered for all reported data. **Supporting Table S4**. XRD parameters related to the structural features of Hard Carbon samples, fitted with OctCarb. **Supporting Table S5**. Deconvolution of the Raman spectra of the pyrolyzed samples and commercial HC. **Supporting Table S6**. XPS surface elemental composition of the prepared samples. **Supporting Table S7**. XPS chemical speciation of the identified elements for the prepared samples. **Supporting Table S8**. Electrochemical performance values and plateau comparison. Reversible capacity (Qrev) and initial coulombic efficiency (ICE).